

# $Ba_{0.5}Gd_{0.8}La_{0.7}Co_2O_{6-\delta}$ Infiltrated $BaZr_{0.8}Y_{0.2}O_{3-\delta}$ Composite Oxygen Electrodes for Protonic Ceramic Cells

**Wang, Qingjie; Ricote, Sandrine; Wang, Yu; Hendriksen, Peter Vang; Wang, Jianqiang; Chen, Ming**

*Published in:*
Journal of the Electrochemical Society

*Link to article, DOI:*
10.1149/1945-7111/ac4934

*Publication date:*
2022

*Document Version*
Peer reviewed version

# $Ba_{0.5}Gd_{0.8}La_{0.7}Co_2O_{6-\delta}$ Infiltrated $BaZr_{0.8}Y_{0.2}O_{3-\delta}$ Composite Oxygen Electrodes for Protonic Ceramic Cells

Qingjie Wang,[1] Sandrine Ricote,[2] Yu Wang,[3] Peter Vang Hendriksen,[1] Jianqiang Wang,[3] and Ming Chen[1,Z]

[1] Department of Energy Conversion and Storage, Technical University of Denmark, Fysikvej, 2800 Kgs. Lyngby, Denmark

[2] Colorado School of Mines, 1500 Illinois Street, Golden, CO 80401, USA

[3] Key Laboratory of Interfacial Physics and Technology, Shanghai Institute of Applied Physics, Chinese Academy of Sciences, Shanghai 201800, China

[Z] minc@dtu.dk

## Abstract

In this study, a composite oxygen electrode is prepared by infiltrating a protonic-electronic conducting material, $Ba_{0.5}Gd_{0.8}La_{0.7}Co_2O_{6-\delta}$ (BGLC) into a proton-conducting $BaZr_{0.8}Y_{0.2}O_{3-\delta}$ (BZY20) backbone. The composite oxygen electrode is studied in a symmetrical cell configuration (BGLC-BZY20//BZY20//BGLC-BZY20). The electrode and cell performance are characterized via electrochemical impedance spectroscopy (EIS) with varying the operating conditions, including temperatures, oxygen, and steam partial pressures, with the purpose to identify and characterize the different electrochemical processes taking place in the oxygen electrode. Three electrode reaction processes are observed in the impedance spectra, which are tentatively assigned to i) diffusion of adsorbed oxygen/proton migration/hydroxyl formation, ii) oxygen reduction, and iii) charge transfer, going from the low- to high-frequency range. The BGLC-BZY20 electrode developed in this work shows a low polarization resistance of 0.22, 0.58, and 1.43 $\Omega$ cm$^2$ per single electrode in 3 % humidified synthetic air (21% $O_2$/79% $N_2$) at 600, 550, and 500 °C, respectively. During long-term measurement, the cell shows no degradation in the first 350 hours but degrades afterward possibly due to insufficient material stability.

## Introduction

Fuel cells and electrolysis cells based on solid oxides – referred to as "solid oxide cells" (SOCs) are promising and efficient devices for energy conversion and storage. Advantages include high energy efficiency, wide fuel options, and modularity.[1,2] Generally speaking, a SOC cell consists of a dense electrolyte sandwiched between two porous electrodes (one oxygen and one hydrogen electrode). Depending on the type of electrolyte, SOCs can be classified as oxygen ion-conducting (O-SOCs) or proton-conducting ceramic cells (PCCs). PCCs are being developed as an alternative to O-SOCs since they offer unique advantages and applications.[3,4] Firstly, due to the lower activation energy for proton transport, PCCs can be operated at lower temperatures (400-600 °C) compared to O-SOCs (typically 700-900 °C). This allows for a more flexible materials selection as well as possibly better durability. In addition, the lower operating temperature enables stack cost reduction and eases challenges related to sealing.[5,6,7] Secondly, the degradation of the Ni-network and Ni redistribution in the hydrogen electrode, which is challenging for O-SOCs, is less critical for PCCs.[8] Thirdly, dry and pure hydrogen can be directly produced and even pressurized in protonic ceramic electrolysis cells (PCEC)

without further gas separation.[9] Therefore, PCCs appear as a promising next-generation technology for renewable energy conversion and storage.

A PCEC is a protonic ceramic fuel cell (PCFC) operated in reverse mode to produce hydrogen. The electrolyte and the hydrogen electrode of PCECs are similar to those for PCFCs; e.g. $BaZr_xY_{1-x}O_{3-\delta}$ (BZY),[10] $BaCe_{0.9-x}Zr_xY_{0.1}O_{3-\delta}$ (BCZY),[11] and $BaCe_{0.8-x}Zr_xY_{0.2-y}Yb_yO_{3-\delta}$ (BCZYYb)[12] for the electrolyte and mixtures of these with Ni for the hydrogen electrode. The oxygen electrode is very important for the overall cell performance and durability. The high oxygen and steam activity prevailing here during operation impose very stringent requirements on the material. In addition, the lower operating temperature in the PCEC (below 600 °C) leads to higher oxygen electrode polarization resistance ($R_P$) due to the thermally activated nature of the electrode processes. The sluggish reaction kinetics at the oxygen electrode is a major challenge for further improvement of PCC's performance.[13,14] Thus, developing robust oxygen electrode materials and structures with high catalytic activity and chemical stability is imperative for the development of commercial PCCs operated at 400-600 °C.

The main role of the PCCs oxygen electrode is to provide the sites for the electrochemical reactions – the oxygen reduction reaction (ORR)/oxygen evolution reaction (OER), and the water-splitting reaction (WSR). Also, it must provide sufficient electronic conductivity for current collection. In PCFC mode, the protons transport through the electrolyte and react with oxygen forming steam on the oxygen electrode side. In contrast to a typical O-SOFC where steam is generated at the hydrogen electrode, producing steam at the oxygen electrode in PCFC improves fuel utilization and efficiency. Furthermore, the absence of steam on the fuel electrode slows down Ni agglomeration, which is currently limiting the lifetime of O-SOECs at high current densities.[15] In PCEC mode, steam is dissociated into oxygen and protons at the oxygen electrode under a current supply, and pure and dry hydrogen is evolved at the hydrogen electrode. Compared with the oxygen electrode reaction processes in O-SOCs, the protons play an important role for proton transfer during the oxygen electrode reaction processes in PCCs. In the choice of materials and in optimizing electrode microstructure, it is beneficial to seek to extend the reaction sites as much as possible - preferably to the whole electrode surface. Otherwise, the ORR/OER and WSR reactions can only take place at the interface between the oxygen electrode and the electrolyte, leading to poor performance as well as potential problems with electrode delamination.[16]

A suitable oxygen electrode should possess the required chemical stability, sufficient porosity, and be chemically compatible with the electrolyte material. A thermal expansion coefficient (TEC) matching reasonably well with that of electrolyte material is desirable to avoid excessive thermo-mechanical stress. Moreover, to minimize the polarization resistance, the oxygen electrode materials should possess sufficient electronic and ionic conductivity as well as good catalytic activity at low operating temperatures. Long-term stability (both chemical and microstructural) is also required. Many high-performance oxygen electrode materials originally developed for O-SOCs have been tested for PCCs, including (1) cubic-type perovskite oxides ($ABO_3$), $Sm_{0.5}Sr_{0.5}CoO_{3-\delta}$ (SSC),[17] $La_{0.6}Sr_{0.4}Co_{0.2}Fe_{0.8}O_{3-\delta}$ (LSCF),[18] and $Ba_{0.5}Sr_{0.5}Co_{0.8}Fe_{0.2}O_{3-\delta}$ (BSCF),[19,20] (2) Ruddlesden–Popper (RP) phase oxides ($A_{n+1}B_nO_{3n+1}$), rare-earth nickel oxides such as $La_2NiO_{4+\delta}$ (LNO)[21] and $Pr_2NiO_{4+\delta}$ (PNO)[22] and (3) double-perovskite oxides ($AA'B_2O_6$), $Sr_2Fe_{1.5}Mo_{0.5}O_{6-\delta}$ (SFMO),[23] $GdBaCuCoO_{5+\delta}$ (GBCC),[24] $PrBa_{0.5}Sr_{0.5}Co_2O_{5+\delta}$ (PBSC).[25] Recently, Vøllestad et al. proposed a novel oxygen

electrode material, $Ba_{0.5}Gd_{0.8}La_{0.7}Co_2O_{6-\delta}$ (BGLC).[26] The partial substitution of Ba with Gd and La results in low apparent polarization resistance and high electronic conductivity. Additionally, this material shows considerable proton conductivity in humidified atmospheres.[27,28]

Besides the intrinsic material properties also the electrode microstructure affects the electrode performance. The electrode activity can be enhanced by maximizing the total surface area available for the reaction using, for example, the following approaches: (a) Preparing composite electrodes by mixing two or more phases with different conduction properties, typically a proton-conducting phase with an electronic or oxygen ion or mixed conducting phase,[29] (b) Impregnating an electrode "backbone" with suitable electro-catalysts,[30] (c) In-situ exsolution of catalytically active nano-particles,[31] or (d) Incorporating high surface area nanofibers (e.g. made by electrospinning). Also, good results on inserting an extra functional layer between the oxygen electrode and the electrolyte by thin film deposition techniques have been found.[32,33]

Figure 1 shows the possible reaction paths at the PCCs oxygen electrode when using a mixed (oxygen ion) ionic and electronic conducting (MIEC) phase, or a mixed protonic and electronic conducting (MPEC) phase, mixed with a proton-conducting ceramic. In an oxygen electrode made of a MIEC+PCC composite (Figure 1a,c), the triple-phase boundaries (TPB) are limited to the electrode-electrolyte interfaces. By replacing the MIEC with an MPEC, the TPB sites for the ORR/OER and WSR are extended to the whole surface of the MPEC phase. In addition, the MPEC oxygen electrode material introduces two potential pathways for proton transport to the electrolyte: A surface pathway and bulk pathway, both impacting the electrochemical activity (Figure 1b, d).

Previous studies have also attempted to describe the overall oxygen electrode reaction mechanism and the rate-determining step(s) for various electrode materials, such as $Sm_{0.5}Sr_{0.5}CoO_{3-\delta}$ (SSC),[34,35] $La_{0.6}Sr_{0.4}Co_{0.2}Fe_{0.8}O_{3-\delta}$ (LSCF),[36] and $BaCo_{0.4}Zr_{0.1}Fe_{0.4}Y_{0.1}O_{3-\delta}$ (BCZFY),[37] but without coming to a simple consensus. Table 1 summarizes possible elementary reaction steps at the oxygen electrode for PCCs as reported in the literature.[38,39,34] The polarization resistance can, in general, be fitted using a power law, $R_i \alpha (P(O_2))^{-m}(P(H_2O))^{-n}$, where $m$ and $n$ are the apparent reaction order of $R_i$ with respect to $P(O_2)$ and $P(H_2O)$. Representative $m$ and $n$ values in PCFC mode have been reported by He et al.[34] for an SSC-$BaCe_{0.8}Sm_{0.2}O_{3-\delta}$ (BSC) electrode.

In this work, we report on a composite oxygen electrode developed by infiltrating a mixed protonic-electronic conducting oxide, BGLC, into a proton-conducting $BaZr_{0.8}Y_{0.2}O_{3-\delta}$ (BZY20) backbone. The BGLC catalyst is introduced into the electrode structure by solution infiltration. This ensures: (1) that the particle size of the infiltrated catalyst can be kept in the sub-100 nm range, which creates a large surface area; (2) that extra surface area can be introduced without sacrificing the mechanical compatibility between the electrode and the electrolyte (both are BZY20); and, finally (3) that cation inter-diffusion between the two phases, that would occur during electrode firing, which takes place at much higher temperatures, is avoided. The manufactured electrodes are characterized by electrochemical impedance spectroscopy under various conditions to elucidate performance-limiting processes.

## Experimental

***Sample Preparation.*** The symmetrical cells studied in this work consist of a dense BZY20 electrolyte and two identical BGLC-BZY20 electrodes. The BZY20 electrolyte pellets were prepared by solid-state reactive sintering, as described in previous work.[40] Shortly, the mixture of precursors (barium carbonate (Alfa Aesar, 99.8%), zirconium oxide (Alfa Aesar, 99+%), and yttrium oxide (Alfa Aesar, REacton ® 99.9% (REO)) was ball-milled with 1 wt.% of NiO, and then was pelletized by uniaxially pressing at 88 MPa for 10s, and followed by sintering at 1550 °C for 6 h on a bed of BZY20 powder. After sintering, the pellets were polished down to a thickness of ~ 800 μm. The BZY20 precursor powder for the electrode backbone was prepared by solid-state reaction using stoichiometric amounts of precursors as in solid-state reactive sintering, but with no addition of NiO. The mixture of the precursors was calcined at 1400 °C for 24 h. The electrode backbone slurry was prepared by mixing the pre-synthesized BZY20 powder with 4 wt.% NiO and 3 wt.% ethylcellulose in alpha-terpineol. Subsequently, the slurry was painted on both sides of the BZY20 electrolyte pellets and fired at 1350 °C in air for 3 h to form a porous BZY20 backbone structure. Electrolyte-supported porous BZY20 // dense BZY20 // porous BZY20 symmetrical cells with a geometrical electrode area of 0.65 $cm^2$ per side were thus obtained.

The BGLC infiltration solution with a concentration of 0.3 mol $L^{-1}$ was prepared as follows: (1) First, stoichiometric amounts of $BaCO_3$ with a purity of 99.8% (wt.%), $Gd(NO_3)_3{\cdot}6H_2O$ (99.9%), $La(NO_3)_3{\cdot}6H_2O$ (99.9%), and $Co(NO_3)_2{\cdot}6H_2O$ (98%) were dissolved in deionized water. (2) The complexation agent of ethylenediaminetetraacetic acid (EDTA, 99%) and citric acid (99.5%) were added according to a molar ratio of EDTA/citric acid/metal ions = 1:2:1. (3) After the pH value was adjusted to 7 by adding appropriate amounts of ammonia water (28%), the solution was stirred continuously for 2 h during heating (80 °C) to form a precursor solution. A surfactant, Pluoronic® P123 (1.7 wt. %), was added to improve the wetting/penetration properties of the solution. Afterward, the BZY20 backbones were infiltrated with the BGLC solution. After the solution spread over the entire surface and was sucked into the pores of the backbone by capillary forces, the samples were calcined at 300 °C in air for 15 min. The above infiltration process was repeated 7 times to reach a loading of 1150 mg of BGLC catalyst per cubic centimeter of BZY20 backbone. Based on a theoretical density of 7.33 g $cm^{-3}$ for BGLC, the fraction of BGLC phase in the BGLC-BZY20 composite electrode is calculated as 15.6 vol.%. The BZY20 accounts for 70 vol.%, whereas the pore phase accounts for 30 vol.% before infiltration and 14.4 vol.% after. The final heat treatment was performed at 700 °C in air for 2 h to obtain the desired nano-crystalline phase of BGLC. In addition, some portion of the BGLC infiltration solution was heated in a crucible at 700 °C for 2 hours, and the obtained powder was used for phase analysis.

***Electrochemical Characterization.*** The electrochemical performance and durability of the symmetrical cells were tested in an in-house built one-atmosphere testing rig, as described in previous work.[41,42] To perform electrochemical measurements, Pt paste was used as the current collector on both electrodes. The cells were heated in dry synthetic air ($21\%O_2/79\%N_2$) to 600 °C with a heating rate of 1 °C $min^{-1}$. The electrochemical performance of the cells under various oxygen and steam partial pressures was evaluated in the temperature range between

500 and 600 °C. To ensure that the samples were at equilibrium when collecting spectra, a dwelling time of 2 h was employed after each change in conditions. The oxygen partial pressure was controlled by adjusting the flow rate ratios of $N_2/O_2$. The total gas flow to the setup was kept at 100 mL $min^{-1}$. The steam was produced by passing the feed gas flow through a water bubbler, and the steam content was varied by adjusting the temperature of the water bubbler between 25 and 50 °C. The electrochemical performance of the cells was characterized by electrochemical impedance spectroscopy (EIS) using a Solartron 1260 frequency response analyzer at frequencies from 96485 to 0.06 Hz with an amplitude of 0.33 V. The in-house developed Python-based software Ravdav was used for plotting and analyzing the EIS data.[43]

***Structure Characterization.*** The prepared materials were analyzed after each synthesis step by X-ray diffraction (XRD, Rigaku Minflex 600) with a scanning range from 20-80°. The microstructure and morphology of "hand-broken" fractured cross-sections of the cells were investigated using a field emission scanning electron microscope (FE-SEM, Zeiss Ultra) with an acceleration voltage of 10 kV. Conductive tape was used to connect the cell to the SEM sample holder in order to minimize charging. Transmission electron microscopy (TEM) and energy-dispersive X-ray spectroscopy (EDS) characterizations were carried out using a Tecani-G2 T20 and F20 operated at an acceleration voltage of 200 kV. The samples for TEM measurements were prepared based on the standard lift-out procedure using a Zeiss Crossbeam 540 dual-beam system equipped with an Oxford OmniProbe 400 micromanipulator.

**Results and Discussion**

***Phase and Microstructure Analysis.*** Figure 2 presents the XRD patterns of the as-synthesized BGLC powder (2h, 700 °C), the BZY20 backbone, and the BGLC-BZY20 composite electrode. High purity single-phase BGLC was obtained from the synthesized BGLC power, as confirmed by the XRD patterns reproduced in Figure 2a. The diffractogram in Figure 2b was collected on a BZY20//BZY20//BZY20 symmetrical cell (prior to infiltration), where only the BZY20 phase is observed. Figure 2c shows the X-ray diffraction pattern of the BGLC infiltrated BZY20 composite electrode calcined at 700 °C in air for 2 h. Peaks corresponding to pure phases of BZY20 and BGLC are identified. Small peaks at 32.5, 45, and 75° are also present in Figure 2c and could be assigned to a perovskite phase $(La,Gd)CoO_3$. It appears that 2h at 700 °C does not result in 100 % phase pure BGLC in the composite BGLC-BZY20 electrode, even though a similar heat treatment of the infiltration solution alone produces pure BGLC (Figure 2a).

Figure 3 presents SEM images on the fractured cross-sections of symmetrical cells without and with infiltration. As illustrated in Figure 3a, a dense BZY20 electrolyte without noticeable pores or cracks is obtained, and the adhesion between the BZY20 electrolyte and the backbone electrode appears to be satisfactory. Figure 3b presents a high magnification SEM micrograph of the porous backbone, which reveals a fairly uniform microstructure suitable for catalyst infiltration and gas diffusion. Figures 3c, d display the BGLC-BZY20//BZY20 interface and a high magnification of the BGLC-BZY20 composite electrode, respectively. No visible changes in the backbone morphology or the adhesion are observed after infiltration (Figure 3c). BGLC nano-particles (50 ~100 nm) are well deposited on the inner surfaces of the porous BZY20 backbone (Figure 3d), providing a continuous porous film with a thickness of

~0.1 μm. Distinct particles/grains can be observed in the film, and the catalyst coating increases the overall surface area available for the electrode reactions as targeted**.**

***Electrochemical Performance at Different Temperatures.*** EIS measurements were carried out on the infiltrated symmetrical cells in 3% humidified synthetic air (21% $O_2$/79% $N_2$) in the temperature range 600-500 °C. The corresponding Nyquist plots are reproduced in Figure 4a. To deconvolute the overall impedance into different reaction processes, an equivalent circuit model consisting of a resistance and an inductance element ($L$-$R_S$) in series with three series connected $R$CPE elements ($R$CPE: a resistor ($R$) in parallel connection with a constant phase element (CPE)) was used to fit the EIS data: $LR_S(R_1CPE_1)(R_2CPE_2)(R_3CPE_3)$. The first and second arcs ($R_1$, $R_2$) have pseudo-capacitances $C$ of $10^{-6} \sim 10^{-4}$ F cm$^{-2}$ and summit frequency between 10 kHz to 500 Hz, are referred to as the high- and medium-frequency processes, respectively. The third arc ($R_3$) with a $C$-value of $10^{0} \sim 10^{-1}$ F cm$^{-2}$ and a frequency range between 0.1 and 1 Hz is referred to as the low-frequency process. The sum of $R_1$+$R_2$+$R_3$ corresponds to the total polarization resistance ($R_P$). It is important to note that all the polarization resistance values listed in this work include contributions from both electrodes unless mentioned differently and specifically referred as to 'single electrode' values. As shown in Figure 4a, the $R_P$ for the two infiltrated BGLC-BZY20 backbone electrodes are 0.44, 1.17, and 2.87 Ω cm$^2$ (0.22, 0.58, and 1.43 Ω cm$^2$ per single electrode) in 3 % humidified synthetic air at 600, 550, and 500 °C, respectively. Strandbakke et al.[27] characterized a BGLC//$BaZr_{0.7}Ce_{0.2}Y_{0.1}O_{2.95}$ (BZCY)//BGLC symmetrical cell and reported an electrode polarization resistance of 0.28 Ω cm$^2$ (per single BGLC electrode) at 600 °C under wet $O_2$/Ar atmosphere ($P(O_2)$ = 0.23 atm). Vøllestad et al.[26] have measured the total cell polarization resistance of a Ni-BZCY//BZCY//BGLC-BZCY single cell for steam electrolysis and found it to be 0.8 Ω cm$^2$ at 600 °C. In their study, the BGLC-BZCY composite oxygen electrode was prepared by mixing 60 vol.% BGLC and 40 vol.% BZCY. Though no further splitting of the different contributions to the cell resistance was reported, one can get a rough estimate using the literature reported polarization resistance of the Ni-BZCY ($BaZr_{0.1}Ce_{0.8}Y_{0.1}O_{3-\delta}$) electrode at 600 °C (0.47 Ω cm$^2$).[44] This gives an estimated value of 0.33 Ω cm$^2$ for the polarization resistance of BGLC-BZCY. Even though the anode polarization resistances estimated from a dual-atmosphere cell testing and from symmetrical cell testing are not 1:1 comparable, the values are in fair agreement. Due to the mixed conductivity nature of the electrolyte, the polarization resistance of the oxygen electrode deduced from symmetrical cell testing is often underestimated.[45] This issue is more severe in oxidizing atmosphere or at high temperatures, as under these conditions the electronic contribution of the electrolyte conductivity is becoming more significant. Thus, caution must be taken when interpreting symmetrical cell test results, though the usual practice reported in literature is to neglect the electronic conductivity in the electrolyte (i.e., the electrolyte is assumed to be a pure proton conductor).[27] Transport numbers for the here applied electrolyte material can be found in literature[46] as can be a defect model accounting for the partial pressure and temperature dependence of the transport number.[47] Especially at 600 °C in air the electronic conductivity becomes non-negligible – meaning that measured $R_P$ values at 600 °C are under-estimated and that apparent $R_P$ and $R_S$ activation energies in the 500-600 °C interval are slightly overestimated. We thus conclude that the performance of our infiltrated electrode is in a similar range as that of the composite electrode

reported by Vøllestad et al.[26] It is, however clear that infiltration reduces the amount of the BGLC phase significantly, from 60 vol.% in the BGLC-BZCY composite electrode to <15.6 vol.% in our infiltrated electrode. This is clearly an advantage. It should be mentioned that we calculated the fraction of BGLC phase based on the measured BGLC loading (1150 mg per $cm^3$ electrode backbone). The real fraction of BGLC phase in composite BGLC-BZY20 after final heat treatment (700 °C in air for 2 h) should be less than 15.6 vol.% due to the decomposition of organic compounds added in the infiltration solution. A more precise determination of the fractions of the different phases in the infiltrated electrode can probably be achieved by reconstruction of the 3D electrode structure using focused ion beam scanning electron microscopy (FIB-SEM) and following structure analysis. Infiltration could also introduce other synergetic effects such as interfacial structure changes or the formation of an interfacial layer between BGLC and BZY20. This requires, however, detailed TEM studies and/or density function theory simulations and shall be pursued in our future work.

The activation energies of $R_S$ and $R_P$ were calculated based on Arrhenius equation, as shown in Figure 4b. The activation energy of $R_S$, the pure ohmic part of the impedance, is 0.44 eV, which is within the range of activation energies reported for typical proton-conducting oxides (0.3-0.6 eV).[48] The apparent activation energies for $R_1$, $R_2$, and $R_3$ derived from Figure 4a are 1.15, 0.76, and 1.42 eV, respectively.

***Electrochemical Performance at Different P($O_2$).*** To further investigate the nature of different resistance contributions, the electrodes were characterized under different oxygen partial pressures at 500 °C. The spectra were fitted as previously with the $LR_S(R_1CPE_1)(R_2CPE_2)(R_3CPE_3)$ equivalent circuit model. Figure 5a shows the impedance spectra of the symmetrical cells at 500 °C with varying the $O_2/N_2$ ratio from 100/0 to 1/99. Both $R_S$ and $R_P$ increase with decreasing $P(O_2)$. In addition to its protonic conductivity, BZY20 also exhibits an electronic contribution (through O-site polarons) in oxidizing atmospheres. It is speculated that the oxidation state of Co in the BGLC phase may affect the ORR/OER. In general, the oxygen exchange reaction rate on oxide electrodes increases with increasing $P(O_2)$. The $P(O_2)$ may also affect the reaction rate via its effect on the hole concentration in the electrode, which increases with increasing $P(O_2)$.[26] Figure 5b represents the isothermal analysis of $R_P$, $R_1$, $R_2$, and $R_3$ resistance contributions as a function of $P(O_2)$ at constant $P(H_2O)$ (~ 3%).

***Electrochemical Performance at Different P($H_2O$).*** In this work, impedance spectra were also recorded with three different degrees of humidification: 3%, 5%, and 10% at 500 °C in synthetic air. A low temperature of 500 °C was chosen to ensure that the proton conduction plays a dominant role in the ionic conduction and to limit the electronic conductivity in oxidizing atmosphere.[49] The experimental and fitted impedance spectra are presented in Figure 6a. The results clearly show a decrease in the oxygen electrode performance with increasing the steam content. This trend was already observed for LSCF, $LaCoO_3$, and $Pr_{0.58}Sr_{0.4}Fe_{0.8}Co_{0.2}O_{3-\delta}$ (PSCF).[50,51,52] The increase in total polarization resistance with $P(H_2O)$ could be related to the presence of steam at the TPBs: the surface sites may be occupied by adsorbed steam, hindering electrochemical reaction processes. Under varying $P(H_2O)$, the same three electrode reaction processes ($R_1$, $R_2$, and $R_3$) are identified. The dependence of the different contributions on $P(H_2O)$ is illustrated in Figure 6b.

***Interpretation of the different semi-circles***. The different arcs were tentatively assigned to the different reaction steps according to the associated pseudo-capacitance values ($C$), their temperature dependence, and the $P(O_2)$ and $P(H_2O)$ dependences. First, all the processes are thermally activated. Therefore, they are not associated with mass transport processes in the gas phase as the latter would be virtually temperature-independent.[53] The capacitance value can give a fingerprint for whether the process is related to an interface, the surface, or process in the bulk.[54] Based on the above-reported capacitance values in the high- and low-frequency range, $R_1$ and $R_2$ likely represent interfacial processes, and $R_3$, due to its much higher capacitance, is likely associated with a surface exchange reaction.[55,52,49]

Starting from the low-frequency, $R_3$ corresponds to a strongly thermally activated process ($E_a$ = 1.42 eV) and has an $m$ exponent of about 0.2. This is close to the value of 0.25 found for diffusion of adsorbed oxygen to the triple-phase boundaries (See Table 1). Geffroy et al.[56] and Berenov et al.[57] reported activation energies in the range 140-165 kJ/mol (1.45-1.71 eV) for the oxygen diffusion coefficient of traditional MIECs. The activation energy for $R_3$ lies in this range. This indicates that the low-frequency process could be related to the oxygen diffusion at the electrode surface. The low-frequency contribution resistance decreases with increasing $P(H_2O)$ ($n$=0.21). This value does not correspond to any of the $n$ exponents reported for different elementary steps in Table 1. The other two contributions ($R_1$ and $R_2$) exhibit a resistance increase with increasing $P(H_2O)$, making the $P(H_2O)$ dependencies challenging to interpret. Nevertheless, a decrease of the resistance with increasing $P(H_2O)$ could be related to the proton migration or hydroxyl formation as both these processes will be facilitated with increasing steam activity. Consequently, the low-frequency process ($R_3$) can either be attributed to the diffusion of adsorbed oxygen, or proton migration or hydroxyl formation.

With regard to the middle frequency, the process related to $R_2$ (500 Hz, $10^{-4}$ F cm$^{-2}$) is weakly dependent on $P(O_2)$ ($m$=0.11) and is thermally activated. In addition, the process has a negative dependence on $P(H_2O)$. According to Table 1 and judging from the observed weak $P(O_2)$ dependence only the most probable process related to $R_2$ would be the oxygen reduction $O^-_{(TPB)} + e^- \rightarrow O^{2-}_{(TPB)}$. As a speculation, this process, that occurs on the surface, could somehow be impeded by adsorbed steam on the same sites leading to the negative n-value. The high frequency ($R_1$, 10 kHz, $10^{-6}$ F cm$^{-2}$) is more complex to assign as the $m$ exponent does not correspond to any of the steps in Table 1 ($m$=0.05). But one should remember that these steps and dependences were developed on composite electrodes made out of the proton-conducting phase and a traditional oxide ion MIEC (SSC-BSC). In our study, BGLC is mainly a proton and electron conductor. Strandbakke et al.[27] allocated this high-frequency contribution to charge transfer from the electrode to the electrolyte. Further studies are needed for a better understanding of these electrochemical processes in our composite oxygen electrodes.

***Durability.*** The durability of the oxygen electrodes was further examined under humidified (10% $H_2O$) synthetic air at 600 °C without bias. Figure 7a presents the electrochemical impedance spectra recorded on the symmetrical cell as a function of testing time at this condition. The BGLC-BZY20//BZY20//BGLC-BZY20 cell displays good stability without noticeable degradation within the first 350 h. The cell, however, starts degrading after this period. To enable a quantitative analysis of the different contributions to the cell

degradation, Figure 7b summarizes the resistance values of $R_S$ and resistances associated with each of the electrode processes from the fitting. Initially, the values for $R_1$ (charge transfer from the electrode to the electrolyte), $R_2$ (oxygen reduction), and $R_3$ (diffusion of adsorbed oxygen or proton migration or hydroxyl formation) are 0.23, 0.20, 0.20 Ω $cm^2$, respectively, with $R_1$ being the dominant term (contributing to 37% of total $R_P$). Within the first 350 h, $R_1$ keeps almost constant and then quickly increases to 0.48 Ω $cm^2$ at 480 h, which accounts for 55% of the total $R_P$ (0.88 Ω $cm^2$). On the other hand, the values of $R_2$ and $R_3$ remain unchanged at 0.20 Ω $cm^2$ during long-term stability testing. These results indicate that the degradation of the cell is primarily due to the change of charge transfer process in the electrode. Fractured cross-sections of the tested symmetrical cell were subjected to SEM analysis to seek to clarify the mechanisms behind the observed performance degradation. As shown in Figure 7c, no layer delamination or crack formation is observed in the tested cell. However, exposure to steam seems to cause some decomposition of the electrode materials and the formation of a secondary phase with a sheet-like morphology (flakes) all over the electrode surface (Figure 7d). The formation of secondary phase (flakes) on the surface of the BGLC could well contribute to the observed degradation of the BGLC-BZY20 electrode.

XRD and TEM analyses on the tested BGLC-BZY20 electrode were further carried out to investigate the observed structural/phase changes. Figure 8a presents the XRD plot of the oxygen electrode after testing. The Pt peaks come from the current collector for the symmetrical cell testing. In addition to the BZY20 and BGLC peaks, minor peaks corresponding to $BaCoO_3$ and $BaCO_3$ were also identified. The existence of these secondary phases was further confirmed by high-resolution transmission electron microscopy (HRTEM) images, as shown in Figure 8b-e. The HRTEM analysis on the region with the flake morphology revealed a lattice spacing of 0.29 nm (Figure 8c), consistent with the reported lattice distance of (020) planes in monoclinic $BaCoO_3$ determined from the XRD analysis (0.281 nm). Additionally, a lattice spacing of 0.50 nm was also found (Figure 8d), very close to the lattice spacing of 0.496 nm between the two (110) planes of the monoclinic $BaCoO_3$.[58] Note that $BaCoO_3$ has been demonstrated to have some electrochemical activity when applied as catalyst for oxygen electrodes.[59] Its flake-like morphology structure can further extend the reaction sites. Hence, the $BaCoO_3$ secondary phase formed in the BGLC-BZY20 electrode may not necessarily be detrimental to the electrode performance, but of course, its formation is associated with some changes also to the composition of the BGLC phase, which may result in inferior catalytic properties of this part of the electrode. The EDS mapping shown in Figure 8e also suggests the formation of a carbonate, most likely $BaCO_3$, as also detected by XRD. From this post-mortem analysis, we conclude that the surface of the BGLC phase is covered by $BaCoO_3$ and $BaCO_3$. While $BaCoO_3$ is not necessarily detrimental to the electrode performance, $BaCO_3$ probably inhibits the proton transfer process, which could contribute to the observed electrode performance degradation. In addition, the formation of Ba-carbonate and Ba-cobaltite changes the defect concentrations in the modified BGLC phase due to the Ba leaching out, which could impede the electrode process. Different sources for the carbon in the formed carbonate have been speculated: carbon from the $BaCO_3$ precursor which was not removed due to low sintering temperature (700 °C), carbon residue in the Pt paste, from the water bubbler, or fast uptake from the atmosphere during the cell setup or testing. Further work is being conducted to clarify the origin of the carbon. In any case, the observation of new phases after

the aging test indicates that the material under the imposed $P(O_2)$, $P(H_2O)$ conditions is not completely stable, and that this is likely the origin of the increased polarization resistance.

## Conclusions

In this work, a composite oxygen electrode for PCCs was successfully prepared by infiltrating mixed protonic-electronic conducting $Ba_{0.5}Gd_{0.8}La_{0.7}Co_2O_{6-\delta}$ into proton-conducting BZY20 backbone. The electrochemical performance of the BGLC-BZY20 composite electrode was investigated at different temperatures, $P(O_2)$ and $P(H_2O)$. The electrode polarization resistances of the BGLC-BZY20 oxygen electrode are found to be 0.22, 0.58, and 1.43 Ω $cm^2$ per single electrode in 3 % humidified synthetic air at 600, 550, and 500 °C, respectively. From the impedance spectra, we find that three different reactions/reaction steps are involved in the electrode process. Based on the chemical capacitance values, frequency ranges, and dependences on $P(O_2)$ and $P(H_2O)$, the three electrode reaction processes were tentatively assigned to the diffusion of adsorbed oxygen/proton migration/hydroxyl formation (low frequency), oxygen reduction (middle frequency), and charge transfer (high frequency), respectively. The symmetrical cells were also exposed to a 480 h durability test at 600 °C in 10 % humidified synthetic air. The cell showed no degradation in the first 350 hours but degraded afterward (the resistance increased from 0.63 to 0.88 Ω $cm^2$ over the 130 h). XRD and TEM analyses of the tested electrode show formation of the $BaCO_3$ and $BaCoO_3$ secondary phases. While $BaCoO_3$ might not in itself account for reduced electrode performance, the formation of $BaCO_3$ and the accompanying changes to the parent BGLC-phase would likely be detrimental.

## Author Contributions

Q.J. Wang and M. Chen conceived and designed the work. S. Ricote, P.V. Hendriksen, and M. Chen supervised the research. S. Ricote and Q.J. Wang manufactured cells. Q. Wang conducted electrochemical testing, XRD, SEM, and data analysis. Y. Wang and J.Q. Wang performed HRTEM&EDS. Q.J. Wang drafted the manuscript. All authors reviewed and revised the manuscript.

## Acknowledgments

Qingjie Wang acknowledges financial support from the China Scholarship Council (CSC201807040049) and from DTU Energy.

## References

1. Y. Zhang, R. Knibbe, J. Sunarso, Y. Zhong, W. Zhou, Z. Shao and Z. Zhu, *Adv. Mater.,* **29**, 1700132 (2017).
2. E. Fabbri, D. Pergolesi and E. Traversa, *Chem. Soc. Rev.*, **39**, 4355–4369 (2010).
3. L. Lei, J. Zhang, Z. Yuan, J. Liu, M. Ni and F. Chen, *Adv. Funct. Mater.*, **29**, 1–17 (2019).
4. J. Kim, S. Sengodan, S. Kim, O. Kwon, Y. Bu and G. Kim, *Renew. Sustain. Energy Rev.*, **109**, 606–618 (2019).
5. Z. Gao, L. V. Mogni, E. C. Miller, J. G. Railsback and S. A. Barnett, *Energy Environ. Sci.*, **9**, 1602–1644 (2016).
6. K. Bae, H. S. Noh, D. Y. Jang, J. Hong, H. Kim, K. J. Yoon, J. H. Lee, B. K. Kim, J. H. Shim

and J. W. Son, *J. Mater. Chem. A*, **4**, 6395–6404 (2016).
7. C. Zuo, S. Zha, M. Liu, M. Hatano and M. Uchiyama, *Adv. Mater.*, **18**, 3318–3320 (2006).
8. T. Matsui, R. Kishida, J. Y. Kim, H. Muroyama and K. Eguchi, *J. Electrochem. Soc.*, **157**, B776 (2010).
9. M. Ni, M. K. H. Leung and D. Y. C. Leung, *Int. J. Hydrogen Energy*, **33**, 4040–4047 (2008).
10. K. D. Kreuer, *Solid State Ion.*, **125**, 285–302 (1999).
11. E. Fabbri, L. Bi, D. Pergolesi and E. Traversa, *Energy Environ. Sci.*, **4**, 4984–4993 (2011).
12. L. Yang, S. Wang, K. Blinn, M. Liu, Z. Liu, Z. Cheng and M. Liu, *Sci.,* **326**, 126–129 (2009).
13. T. Z. Sholklapper, H. Kurokawa, C. P. Jacobson, S. J. Visco and L. C. De Jonghe, *Nano Lett.*, **7**, 2136–2141 (2007).
14. J. G. Lee, J. H. Park and Y. G. Shul, *Nat. Commun.*, **5** (2014).
15. M. Chen, Y. L.Liu, J. J. Bentzen, W. Zhang, X. F. Sun, A. Hauch, Y. T. Tao, J. R. Bown and P. V. Hendriksen, *J. Electrochem. Soc*, **160**, 883 (2013).
16. E. Fabbri, D. Pergolesi and E. Traversa, *Sci. Technol. Adv. Mater.*, **11**, 1–9 (2010).
17. F. Zhao, Q. Liu, S. Wang and F. Chen, *J. Power Sources*, **196**, 8544–8548 (2011).
18. L. Lei, Z. Tao, T. Hong, X. Wang and F. Chen, *J. Power Sources*, **389**, 1–7 (2018).
19. D. K. Lim, J. H. Kim, A. U. Chavan, T. R. Lee, Y. S. Yoo and S. J. Song, *Ceram.*, **42**, 3776–3785 (2016).
20. Y. Chen, Q. Gu, D. Tian, Y. Ding, X. Lu, W. Yu, T. T. Isimjan and B. Lin, *Int. J. Hydrogen Energy*, **39**, 13665–13670 (2014).
21. H. Tang, Z. Gong, Y. Wu, Z. Jin and W. Liu, *Int. J. Hydrogen Energy*, **43**, 19749–19756 (2018).
22. W. Li, B. Guan, L. Ma, S. Hu, N. Zhang and X. Liu, *J. Mater. Chem. A*, **6**, 18057–18066 (2018).
23. L. Lei, Z. Tao, X. Wang, J. P. Lemmon and F. Chen, *J. Mater. Chem. A*, **5**, 22945–22951 (2017).
24. X. Zhang, Y. Jiang, X. Hu, L. Sun and Y. Ling, *Electron. Mater. Lett.*, **14**, 147–153 (2018).
25. S. Choi, C. J. Kucharczyk, Y. Liang, X. Zhang, I. Takeuchi, H. Il Ji and S. M. Haile, *Nat. Energy*, **3**, 202–210 (2018).
26. E. Vøllestad, R. Strandbakke, M. Tarach, D. Catalán-Martínez, M. L. Fontaine, D. Beeaff, D. R. Clark, J. M. Serra and T. Norby, *Nat. Mater.*, **18**, 752–759 (2019).
27. R. Strandbakke, V. A. Cherepanov, A. Y. Zuev, D. S. Tsvetkov, D. S, Argirusis, C. Sourkouni, S. Prünte, T. Norby, *Solid State Ion.*, **278**, 120-132 (2015).
28. E. Vøllestad, M. Schrade, J. Segalini, R. Strandbakke and T. Norby, *J. Mater. Chem. A*, **5**, 15743–15751 (2017).
29. J. Dailly, F. Mauvy, M. Marrony, M. Pouchard and J. C. Grenier, *J Solid State Electrochem.*, **15**, 245–251 (2011).
30. D. Ding, X. Li, S. Y. Lai, K. Gerdes and M. Liu, *Energy Environ. Sci.*, **7**, 552–575 (2014).
31. Y. Chen, S. Yoo, K. Pei, D. Chen, L. Zhang, B. deGlee, R. Murphy, B. Zhao, Y. Zhang, Y. Chen and M. Liu, *Adv. Funct. Mater.*, **28**, 1–7 (2018).
32. W. Wu, H. Ding, Y. Zhang, Y. Ding, P. Katiyar, P. K. Majumdar, T. He and D. Ding, *Adv. Sci.*, **5**, 1800360 (2018).
33. S. Choi, C. J. Kucharczyk, Y. Liang, X. Zhang, I. Takeuchi, H. Il Ji and S. M. Haile, *Nat. Energy*, **3**, 202–210 (2018).

34. F. He, T. Wu, R. Peng and C. Xia, *J. Power Sources*, **194**, 263–268 (2009).
35. F. He, D. Song, R. Peng, G. Meng and S. Yang, *J. Power Sources*, **195**, 3359–3364 (2010).
36. E. Fabbri, L. Bi, D. Pergolesi and E. Traversa, *Energy Environ. Sci.*, **4**, 4984–4993 (2011).
37. M. Saqib, J. I. Lee, J. S. Shin, K. Park, Y. D. Kim, K. B. Kim, J. H. Kim, H. T. Lim and J. Y. Park, *J. Electrochem. Soc.*, **166**, F746–F754 (2019).
38. E. Fabbri, A. Magrasó and D. Pergolesi, *MRS Bull.*, **39**, 792–797 (2014).
39. L. Bi, S. Boulfrad and E. Traversa, *Chem. Soc. Rev.*, **43**, 8255–8270 (2014).
40. S. Ricote, N. Bonanos, A. Manerbino and W. G. Coors, *Int. J. Hydrogen Energy*, **37**, 7954–7961 (2011).
41. X. Tong, S. Ovtar, K. Brodersen, P. V. Hendriksen and M. Chen, *ACS Appl. Mater. Interfaces*, **11**, 25996–26004 (2019).
42. X. Tong, P. V. Hendriksen, A. Hauch and M. Chen, *ECS Trans.*, **91**, 2433–2442 (2019).
43. C. R. Graves, Ravdav, *Data Analysis Software, Ver 0.97*, 2012.
44. V. Mao, Novel mixed protonic-electronic materials: Development of selective membranes devoted for hydrogen separation. Ph.D. Thesis, *Montpellier University*, 2016.
45. D Medvedev, *Int. J. Hydrogen Energy*, **44**, 26711-26740 (2019).
46. D. Han, K. Goto, M. Majima and T. Ude, *ChemSusChem*, **14**, 614-623 (2021).
47. H. Zhu, S. Ricote, C. Duan, R. O'Hayre, D. Tsvetkov and R. Jee, *J. Electrochem. Soc.,* **165**, F581 (2018).
48. D. Pergolesi, E. Fabbri, A. D'Epifanio, E. Di Bartolomeo, A. Tebano, S. Sanna, S. Licoccia, G. Balestrino and E. Traversa, *Nat. Mater.*, **9**, 846–852 (2010).
49. T. Nakamura, S. Mizunuma, Y. Kimura, Y. Mikami, K. Yamauchi, T. Kuroha, N.Taniguchi, Y. Tsuji, Y. Okuyama and K. Amezawa, *J. Mater. Chem. A*, **6**, 15771–15780 (2018).
50. A. Grimaud, F. Mauvy, J. M. Bassat, S. Fourcade, L. Rocheron, M. Marrony and J. C. Grenier, *J. Electrochem. Soc.*, **159**, 683–694 (2012).
51. Q. Wang, X. Tong, S. Ricote, R. Sažinas and P. Vang, *Advanced Powder Materials*, (2021) DOI: /10.1016/j.apmate.2021.09.003.
52. V. B. Vert, C. Solís and J. M. Serra, *Fuel Cells*, **11**, 81–90 (2011).
53. F. Mauvy, C. Lalanne, J. M. Bassat, J.C. Grenier, H. Zhao, L. Huo and P. Stevens, *J. Electrochem. Soc.*, **153**, A1547 (2006).
54. S. B. Adler, *Chem. Rev.*, **104**, 4791–4843 (2004).
55. S. Ricote, N. Bonanos, P. M. Rørvik and C. Haavik, *J. Power Sources*, **209**, 172–179 (2012).
56. P. M. Geffroy, E. Deronzier, J. Gillibert, P. Munch, T. Chartier, and J. Fouletier, *J. Electrochem. Soc.*, **167**, 064503 (2020).
57. A. V. Berenov, A. Atkinson, J. A. Kilner, E. Bucher, and W. Sitte, *Solid State Ion.*, **181**, 819–826 (2010).
58. A. Jain, S. P. Ong, G. Hautier, W. Chen, W. D. Richards, S. Dacek, S. Cholia, D. Gunter, D. Skinner, G. Ceder and K. A. Persson, *APL Materials*, **1**, 011002 (2013).
59. Y. Chen, Y. M. Choi, S. Yoo, Y. Ding, R. Yan, K. Pei, C. Qu, L. Zhang, I. Chang, B. Zhao, Y. Zhang, H. Chen, Y. Chen, C. Yang, B. deGlee, R. Murphy, J. Liu and M. Liu, *Joule*, **2**, 938–949 (2018).

## Table

TABLE 1. Possible elementary oxygen electrode reaction steps in PCCs modified after literature [34,39].

| | Process | Elementary reaction | m | n |
|---|---|---|---|---|
| PCEC | Water adsorption | $H_2O_{(g)} \rightarrow H_2O_{(ad)}$ | | |
| | Water dissociation | $H_2O_{(ad)} \rightarrow OH^-_{(ad)} + H^+_{(ad)}$ | | |
| | Hydroxide dissociation | $OH^-_{(ad)} \rightarrow O^{2-}_{(ad)} + H^+_{(ad)}$ | | |
| | Oxygen oxidation | $O^{2-}_{ad} - e^- \rightarrow O^-_{(ad)}$ | | |
| | Oxygen oxidation | $O^-_{(ad)} - e^- \rightarrow O_{(ad)}$ | | |
| | Oxygen formation | $2O_{(ad)} \rightarrow O_{2(ad)}$ | | |
| | Oxygen desorption | $O_{2(ad)} \rightarrow O_2$ | | |
| | Proton transfer | $H^+_{(ad)} \rightarrow H^+_{(TPB)}$ | | |
| | Proton incorporation into electrolyte | $H^+_{(TPB)} \rightarrow H^+_{(electrolyte)}$ | | |
| PCFC | Oxygen adsorption and splitting | $O_{2(g)} \rightarrow 2O_{ad}$ | 1 | 0 |
| | Oxygen reduction | $O_{ad} + e^- \rightarrow O^-_{ad}$ | 3/8 | 0 |
| | Oxygen surface diffusion toward the reaction site | $O^-_{ad} \rightarrow O^-_{TPB}$ | 1/4 | 0 |
| | Oxygen reduction | $O^-_{(TPB)} + e^- \rightarrow O^{2-}_{(TPB)}$ | 0 | 0 |
| | Proton migration toward the reaction site | $H^+_{(electrolyte)} \rightarrow H^+_{TPB}$ | 0 | 1/2 |
| | Hydroxide formation | $H^+_{(TPB)} + O^{2-}_{(TPB)} \rightarrow OH^-_{(TPB)}$ | 0 | 1/2 |
| | Reaction proton/hydroxide to form water at TPB | $H^+_{(TPB)} + OH^-_{(TPB)} \rightarrow H_2O_{(TPB)}$ | 0 | 1 |

Note: No m, n values for PCEC have been reported in literature. The values for PCFC were taken from He et al.[34]

**Figures**

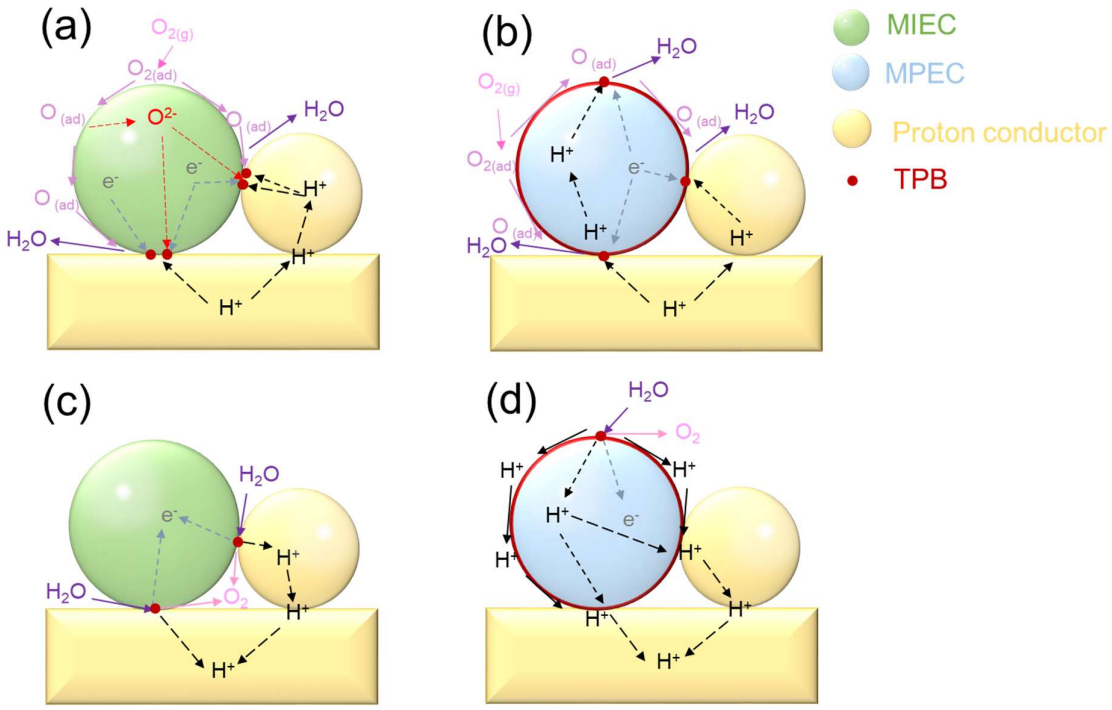


Figure 1. Potential reaction paths at the composite oxygen electrode for PCC, containing a proton-conducting phase and (a, c) a mixed $O^{2-}/e^{-}$ conducting phase (MIEC) or (b, d) a mixed $H^{+}/e^{-}$ conducting phase (MPEC).

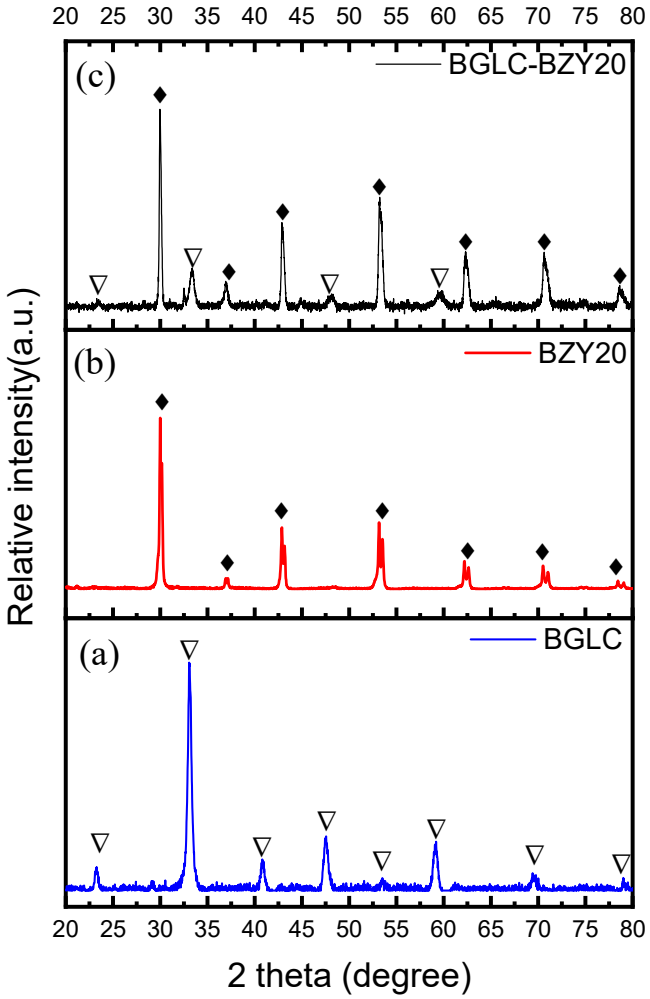


Figure 2. XRD patterns of (a) BGLC powder synthesized from the infiltration solution (700 °C in air for 2 h); (b) the BZY20 electrode backbone; (c) the BGLC infiltrated BZY20 electrode.

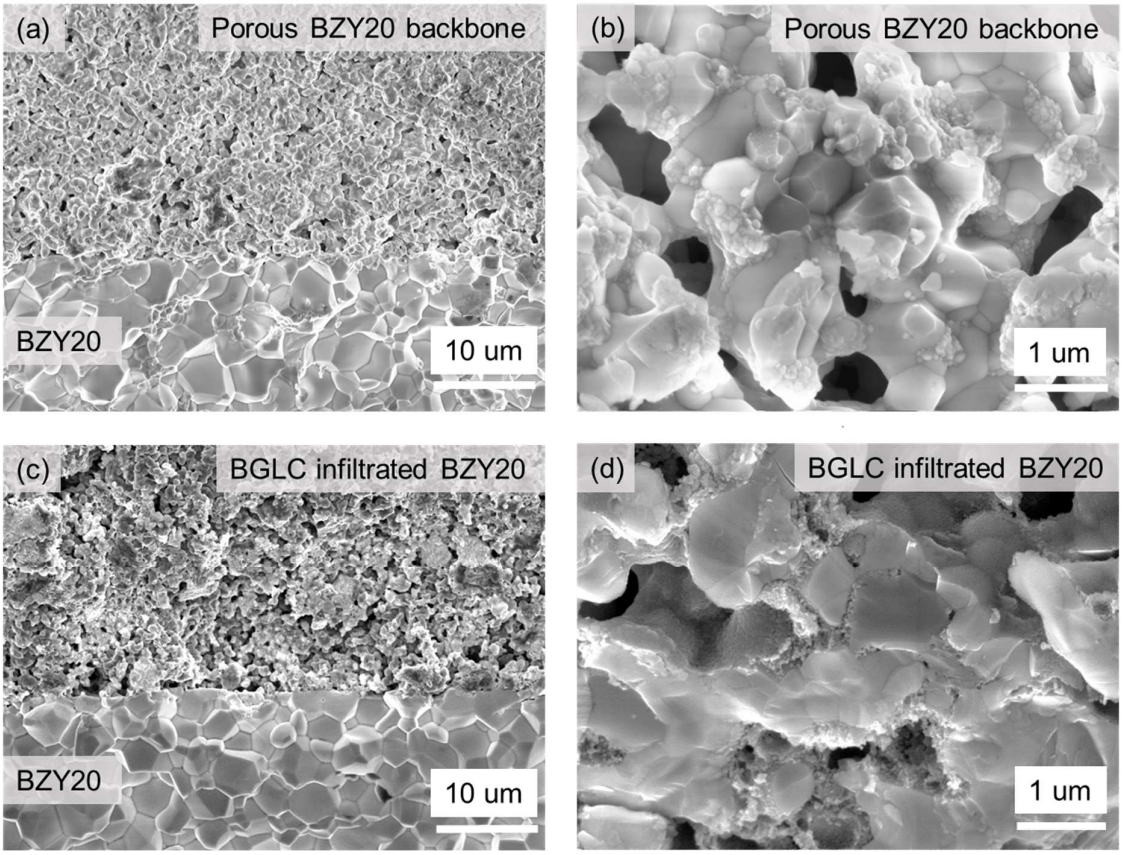


Figure 3. SEM images on the fractured cross-sections of symmetrical cells without and with infiltration showing (a) the interface between BZY20 backbone and BZY20 electrolyte; (b) BZY20 oxygen electrode backbone; (c) the interface between the BGLC infiltrated BZY20 composite oxygen electrode and the BZY20 electrolyte; (d) BGLC infiltrated BZY20 composite oxygen electrode.

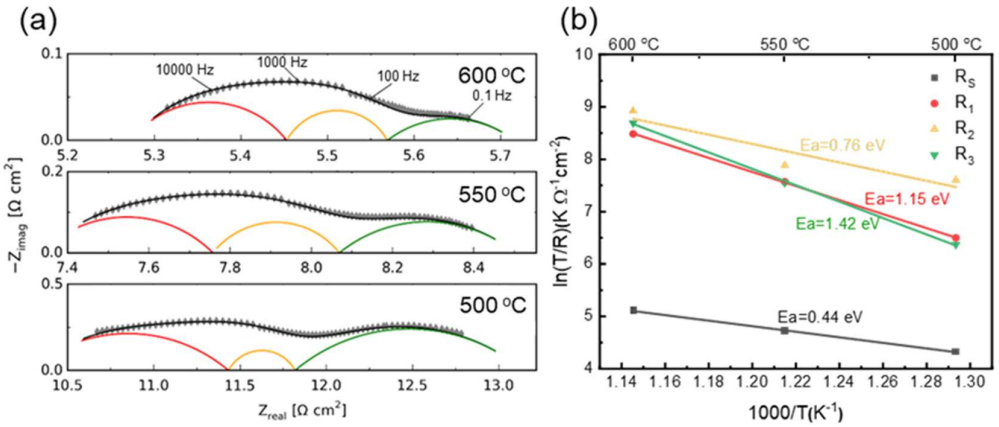


Figure 4. (a) Impedance spectra of the symmetrical cells measured in humidified (3% $H_2O$) synthetic air from 600-500 °C together with fitted spectra using a three-arc equivalent circuit model (closed symbols: experimental data; solid lines: fitted data) and (b) Temperature dependence of the resistances ($R_S$, $R_1$, $R_2$ and $R_3$) derived from the EIS and the calculated

activation energy.

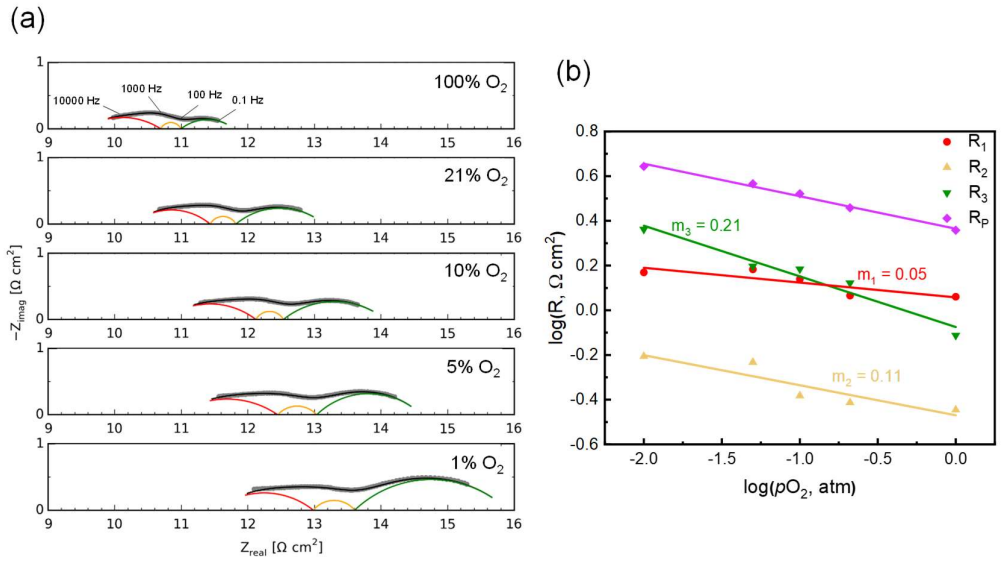


Figure 5. (a) Impedance spectra of the symmetrical cells measured at 500 °C under different oxygen particle pressures $P(O_2)$, always with 3% $H_2O$, together with the fitted curves (closed symbols: experimental data; solid lines: fitted data). (b) Dependence of $R_P$, $R_1$, $R_2$ and $R_3$ as a function of $P(O_2)$ at 500 °C.

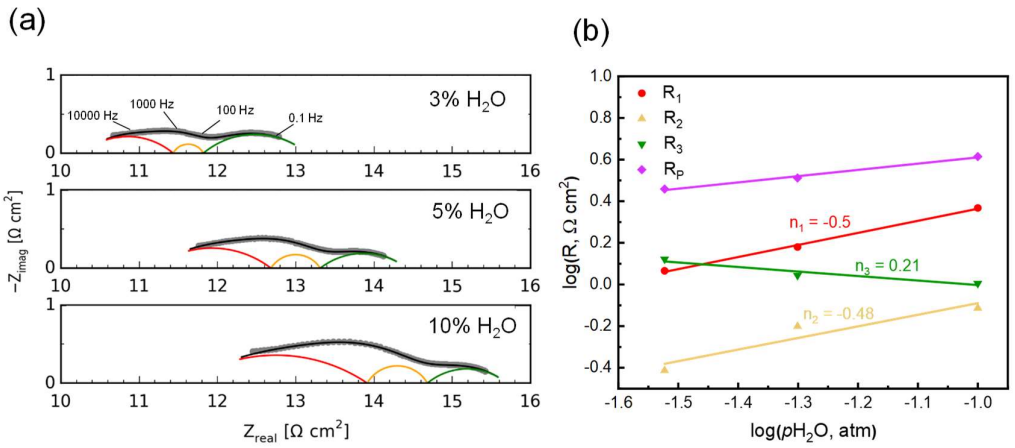


Figure 6. (a) Impedance spectra of the symmetrical cells measured at 500 °C in synthetic air with different $P(H_2O)$, together with fitted curves (closed symbols: experimental data; solid lines: fitted data); (b) Dependence of $R_P$, $R_1$, $R_2$ and $R_3$ on $P(H_2O)$ at 500 °C.

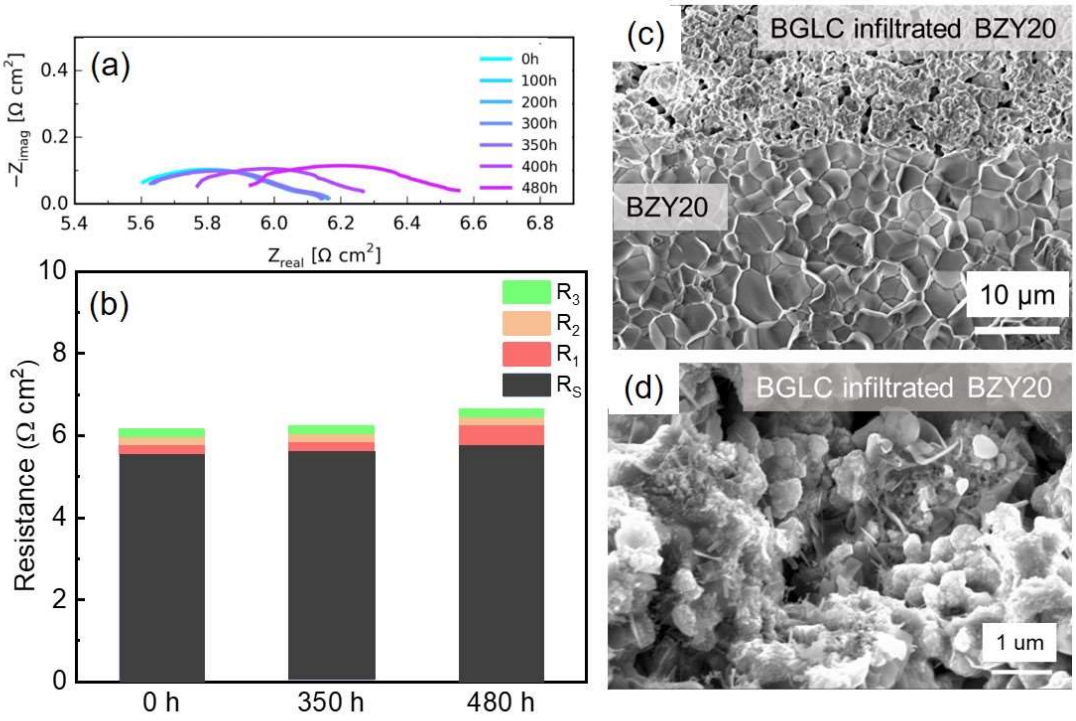


Figure 7. (a) The EIS measured at 600 °C in humidified (10% $H_2O$) synthetic air without bias as a function of time; (b) Resistances from the fitting results; (c) SEM image on the fractured cross-section of the symmetrical cell after the durability testing; and (d) Corresponding high magnification SEM image of the BGLC-BZY20 oxygen electrode (post-test).

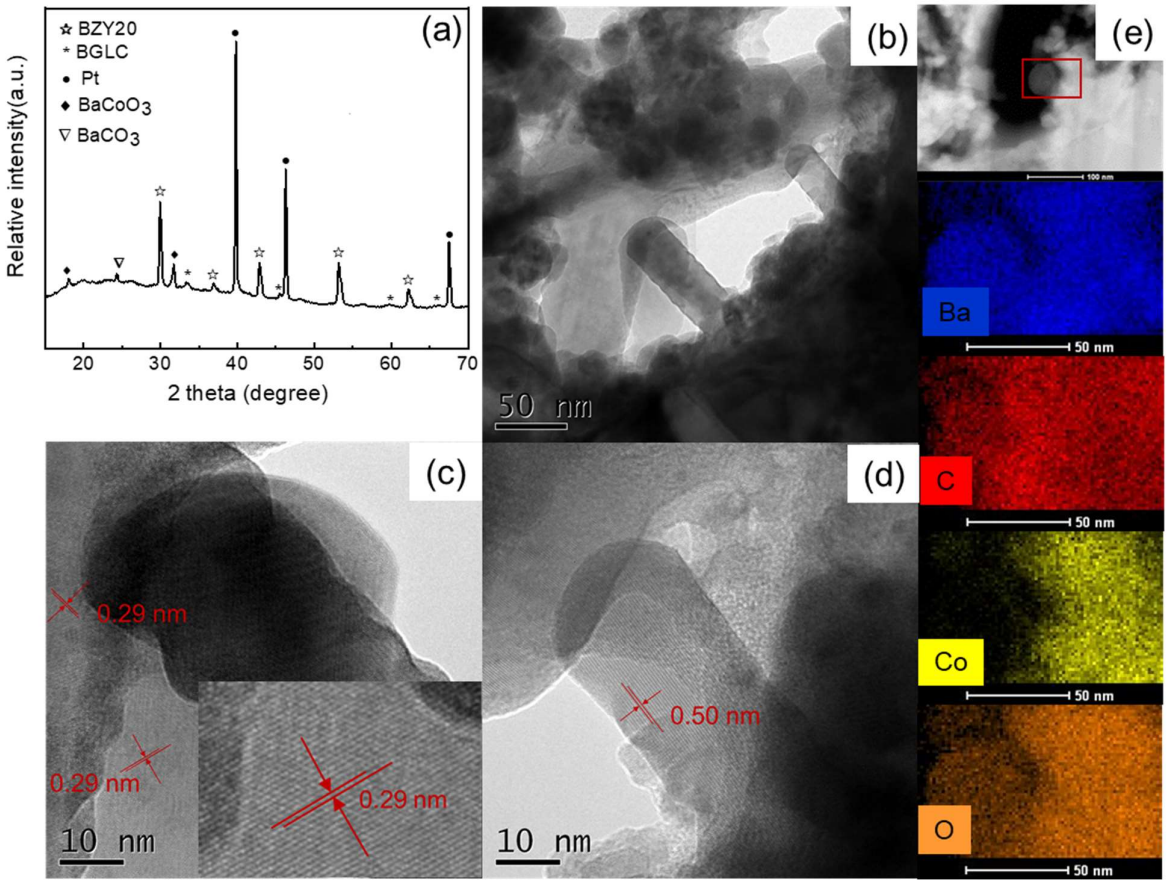


Figure 8. (a) XRD pattern of the BGLC-BZY20 oxygen electrode after long-term testing at 600 °C in humidified (10% $H_2O$) synthetic air; (b) High-resolution transmission electron microscopy (HRTEM) images of the BGLC-BZY20 oxygen electrode; (c) and (d) the sheet-like morphology (flakes) taken from various spots; (e) Energy-dispersive X-ray spectroscopy (EDS) maps of Ba, C, Co, O.

**Figure Captions**

Figure 1. Potential reaction paths at the composite oxygen electrode for PCC, containing a proton-conducting phase and (a, c) a mixed $O^{2-}/e^{-}$ conducting phase (MIEC) or (b, d) a mixed $H^{+}/e^{-}$ conducting phase (MPEC).

Figure 2. XRD patterns of (a) BGLC powder synthesized from the infiltration solution (700 °C in air for 2 h); (b) the BZY20 electrode backbone; (c) the BGLC infiltrated BZY20 electrode.

Figure 3. SEM images on the fractured cross-sections of symmetrical cells without and with infiltration showing (a) the interface between BZY20 backbone and BZY20 electrolyte; (b) BZY20 oxygen electrode backbone; (c) the interface between the BGLC infiltrated BZY20 composite oxygen electrode and the BZY20 electrolyte; (d) BGLC infiltrated BZY20 composite oxygen electrode.

Figure 4. (a) Impedance spectra of the symmetrical cells measured in humidified (3% $H_2O$) synthetic air from 600-500 °C together with fitted spectra using a three-arc equivalent circuit model (closed symbols: experimental data; solid lines: fitted data) and (b) Temperature dependence of the resistances ($R_S$, $R_1$, $R_2$ and $R_3$) derived from the EIS and the calculated activation energy.

Figure 5. (a) Impedance spectra of the symmetrical cells measured at 500 °C under different oxygen particle pressures $P(O_2)$, always with 3% $H_2O$, together with the fitted curves (closed symbols: experimental data; solid lines: fitted data). (b) Dependence of $R_P$, $R_1$, $R_2$ and $R_3$ as a function of $P(O_2)$ at 500 °C.

Figure 6. (a) Impedance spectra of the symmetrical cells measured at 500 °C in synthetic air with different $P(H_2O)$, together with fitted curves (closed symbols: experimental data; solid lines: fitted data); (b) Dependence of $R_P$, $R_1$, $R_2$ and $R_3$ on $P(H_2O)$ at 500 °C.

Figure 7. (a) The EIS measured at 600 °C in humidified (10% $H_2O$) synthetic air without bias as a function of time; (b) Resistances from the fitting results; (c) SEM image on the fractured cross-section of the symmetrical cell after the durability testing; and (d) Corresponding high magnification SEM image of the BGLC-BZY20 oxygen electrode (post-test).

Figure 8. (a) XRD pattern of the BGLC-BZY20 oxygen electrode after long-term testing at 600 °C in humidified (10% $H_2O$) synthetic air; (b) High-resolution transmission electron microscopy (HRTEM) images of the BGLC-BZY20 oxygen electrode; (c) and (d) the sheet-like morphology (flakes) taken from various spots; (e) Energy-dispersive X-ray spectroscopy (EDS) maps of Ba, C, Co, O.